The Astrophysical Journal, 982:47 (14pp), 2025 March 20 https://doi.org/10.3847/1538-4357/adb60c
© 2025. The Author(s). Published by the American Astronomical Society.
OPEN ACCESS

Investigating Coronal Mass Ejections through Multispacecraft Measurements: STEREO-A and L1 in 2022–2023

Sahanaj A. Banu, Noé Lugaz, Bin Zhuang, Nada Al-Haddad, Charles J. Farrugia, and Antoinette B. Galvin
Institute for the Study of Earth, Oceans, and Space, University of New Hampshire, Durham, NH, USA; sahanaj.banu@unh.edu
Received 2024 December 4; revised 2025 January 27; accepted 2025 February 6; published 2025 March 18

Abstract

The angular width of coronal mass ejections (CMEs) and the variations of CME properties for various crossings through the structure remain insufficiently studied and inadequately understood, primarily due to the rarity of multispacecraft measurements. From 2022 January to 2023 August, STEREO-A was in relative proximity to the Sun–Earth first Lagrangian (L1) point, with the STEREO-A–L1 angular separation reducing from 35° to 0°, corresponding to a time with an increasing activity of solar cycle 25 approaching its maximum. This provides a unique time period to obtain multispacecraft measurements of CMEs and to analyze their properties as observed by Wind/ACE and STEREO-A. Among 49 total CMEs measured by either spacecraft over the 20 months, only 15 were simultaneously detected at both spacecraft, indicating that only 31% of CMEs impacted both within a longitudinal separation of 0°–35°. While 80%–100% of CMEs were observed by both spacecraft within 10°, this percentage rapidly dropped to approximately 30% beyond 10°, and near 30°, it fell further to 10%. These findings suggest that the average CME angular width near 1 au is likely between 20°and 35°, smaller than previously suggested. Furthermore, the analysis of these 15 events reveals that average CME properties like magnetic field strength and proton speed are largely consistent regardless of angular separation. However, correlations and rms error analyses highlight significant variability in CME properties even within separations of 10°–20°, when examining their internal variations in detail. This study raises numerous questions about our knowledge of CME properties.

Unified Astronomy Thesaurus concepts: Solar coronal mass ejections (310); Ejecta (453); Interplanetary physics (827)

Materials only available in the online version of record: animation, machine-readable table

1. Introduction

Coronal mass ejections (CMEs) are large magnetic structures embedded in plasma that erupt from the solar surface and then propagate through the heliosphere (e.g., see reviews by W. Manchester et al. 2017; J. G. Luhmann et al. 2020; N. Al-Haddad & N. Lugaz 2025). CMEs are among the most significant drivers of space weather, and their study is essential for improving our understanding of solar–terrestrial interactions and advancing predictive capabilities (E. K. J. Kilpua et al. 2019; J. Zhang et al. 2021). Over the past four decades, extensive research has been conducted using both remote-sensing observations and in situ measurements to characterize these large-scale eruptions from the Sun (e.g., J. T. Gosling 1990; M. Leitner et al. 2007; J. Zhang et al. 2021). The morphology of CMEs can be understood through remote-sensing observations (A. Vourlidas et al. 2013; B. Zhuang et al. 2024). CMEs, when measured in situ near 1 astronomical unit (au), exhibit distinct plasma and magnetic field signatures that differentiate them from the ambient solar wind (L. Burlaga et al. 1981; J. T. Gosling 1990; H. V. Cane et al. 1998; I. G. Richardson & H. V. Cane 2004; L. K. Jian et al. 2018). In in situ measurements, CMEs typically present as a magnetically dominated magnetic ejecta (ME), which is preceded by a sheath region made of compressed solar wind material in approximately 80% of the cases and by a fast forward shock approximately 60% of the time (T. M. Salman et al. 2021). These structures have been observed to have a radial extent of the whole CME of ∼0.3 au near 1 au, comprising the ME (∼0.21 au; see V. Bothmer & R. Schwenn 1998; R. P. Lepping et al. 2005; I. G. Richardson & H. V. Cane 2010) and, if present, the shock and sheath (∼0.09 au; see E. Kilpua et al. 2017; T. M. Salman et al. 2021).

In this article, we used similar terminology as discussed in N. Lugaz et al. (2024a): the whole eruption, irrespective of mode of observation or measurements, is referred to as the CME. The magnetically dominated part is the ME. MEs with some special properties, as described in L. Burlaga et al. (1981), are called magnetic clouds (MCs).

As the CME propagates and expands through the heliosphere, the parameters associated with the CME change, such as density, magnetic field strength, and shock structures (R. M. Winslow et al. 2015). Also, the ME can sometimes rotate (B. J. Lynch et al. 2009), and get deflected (Y. Wang et al. 2014; C. Kay et al. 2015; B. Zhuang et al. 2017, 2019) when it interacts with the solar wind.

Using more than a thousand in situ measurements of CMEs (e.g., see C. Möstl et al. 2017), with spacecraft situated at different radial distances, combined with remote observations, the evolution and properties of CMEs have been studied, as further discussed below. Despite these advances, the full extent of CME structures cannot be adequately captured through single-point observations. Multiple spacecraft, positioned at varying latitudes and longitudes but at similar radial distances, are required to fully probe the three-dimensional nature of CMEs (C. J. Farrugia et al. 2011; E. K. J. Kilpua et al. 2011a;

Original content from this work may be used under the terms of the Creative Commons Attribution 4.0 licence. Any further distribution of this work must maintain attribution to the author(s) and the title of the work, journal citation and DOI.

N. Lugaz et al. 2018; C. Scolini et al. 2021). Multispacecraft measurements thus offer the advantage of capturing the complex geometry of CMEs.

Apart from the structural component of CMEs, multispacecraft measurements at different distances also shed light on the evolution of CMEs with distances. Earlier work by V. Bothmer & R. Schwenn (1998) used data from the Helios, Voyager, and Interplanetary Monitoring Platform (IMP) spacecraft to statistically analyze CME evolution between 0.3 and 4.2 au. This study revealed that the radial diameter of CMEs increases with distance, proportional to $r^{0.8}$, density decreases consistently with size, and highlighted that the longitudinal extent of CMEs could be up to 60°, generally aligning their axes with the ecliptic plane.

Further single-event analyses provide insight into specific CME behaviors. For example, S. W. Good et al. (2015) observed a CME in 2011 November, tracking it from 0.44 to 1.09 au using MESSENGER, Venus Express, and STEREO-B. They found that the CME size increased similarly, as found earlier, and its magnetic field decayed at $r^{-1.84}$, along with significant axial rotation, showing how individual CMEs can exhibit dynamic internal evolution. Additionally, F. Regnault et al. (2023) examined the "aging" effect of a CME detected by two closely spaced spacecraft, finding that interactions with the interplanetary magnetic field (IMF) caused significant asymmetries in the magnetic and velocity profiles, leading to a loss of coherent structure within the ME.

Collectively, these studies underscore how CMEs expand, rotate, decelerate, and undergo structural changes as they propagate, shaped by interactions with the solar wind and interplanetary magnetic field. As a result, we now have a clearer understanding of CME evolution across heliospheric distances through statistical analyses and individual case studies.

However, relatively few investigations have focused on examining the difference in CME properties along nonradial separations in latitude and longitude, despite its importance for improving CME modeling and predictions on impacting Earth (N. Lugaz et al. 2024b). Studying CME angular width in nonradial directions is necessary to comprehend the CME global structure. This has traditionally been possible through remote-sensing observations of coronagraphs that capture the CME bright front and dark cavity structures, which evolve with heliocentric distance. For example, T. A. Howard & C. E. DeForest (2012) found the 2008 December 12 CME latitudinal width to be 39° for the bright front and 31° for the cavity, with longitudinal widths of 56° and 24°, respectively. J. P. Byrne et al. (2010) observed another CME angular width of the bright front to increase from 45° to 60° while propagating from 0.05 to 0.2 au. A stereoscopic method was developed by N. Lugaz (2010) to find longitudinal size; interestingly, they found that the CME longitudinal width decreased from 90° to 70° by 0.5 au for two events. Using the Graduated Cylindrical Shell (GCS) model (A. Thernisien et al. 2009), L. Rodriguez et al. (2011) and X. H. Zhao et al. (2017) found the average longitudinal width to be 51° (when 26 CMEs are used) and the leg-to-leg width to be 48° (using 33 CMEs). For 122 CMEs from the KINCAT catalog,[1] an average leg-to-leg width was found to be 44°.

In situ simultaneous multispacecraft measurements are key for understanding CME angular extent and properties directly, yet simultaneous CME detection at multiple locations has been limited until now due to unavailable preferred spacecraft locations. With the launch of twin STEREO (A and B) satellites, this horizon has been widened, which is discussed in detail by E. K. J. Kilpua et al. (2011a). In this article, six CMEs measured by STEREO and Wind were analyzed for longitudinal separations of 9°–23° from Earth on either side, revealing distinct properties across events and a consistent influence from the surrounding plasma environment. Two events exhibited a longitudinal extent of at least 40°, as all three spacecraft recorded them (see also C. J. Farrugia et al. 2011). However, the launch of STEREO during solar minimum and rapid separation from the Sun–Earth line limited the number of events with simultaneous measurements to only a handful in 2007.

Using a database of ∼400 CMEs as measured by MESSENGER, Venus Express, Wind, ACE, and STEREO, S. W. Good & R. J. Forsyth (2016) found that, for longitudinal separations of up to 15°, two spacecraft had 82% of simultaneous CME detections, while, for separations of 15°–30°, this rate reduced to 49%, and for separations exceeding 60°, no ME was simultaneously detected. With increasing separation, only the sheath was detected at both locations, and no ME was measured, implying that CME flux ropes (FRs) are narrower than the shocks they drive. This study used spacecraft at different heliocentric distances, while the CME radial evolution can affect the arrival/hit of the CME at different spacecraft. In addition, MESSENGER and Venus Express only had magnetic fields but no plasma measurements, which affects the reliability of CME identification, especially when the magnetic field measurements are different. An earlier work by H. V. Cane et al. (1997) used Helios 1, Helios 2, and IMP 8 to examine CME ejecta at separations up to 53°, observing only a few ejecta within a 40° separation and none beyond.

The launch of the Parker Solar Probe (PSP) and Solar Orbiter enabled a few additional such measurements. R. M. Winslow et al. (2021) examined a slow, initially weak CME detected by the PSP and STEREO-A with an angular separation of approximately 8°. Over a radial distance of about 0.12 au, this CME maintained steady acceleration, potentially driven by interaction with a high-speed solar wind stream (HSS). These findings highlight how interactions with corotating solar wind structures can influence CME morphology and propagation characteristics and how the CME properties can vary within smaller longitudinal and radial separations (F. Regnault et al. 2023, 2024).

The first article to study the correlation between CME parameters along a nonradial distance for small separations highlighted diminishing magnetic field correlations with increased spacecraft separations, challenging traditional CME core models and raising concerns about our understanding of CME structure (N. Lugaz et al. 2018). Expanding on this, M. Ala-Lahti et al. (2020) measured coherence lengths in CME sheaths, finding longer coherence scales in sheaths than the surrounding solar wind. Recently, N. Lugaz et al. (2024a) analyzed all CMEs that propagate from the Sun between the Sun–STEREO-A and Sun–Earth line in 2021–2022 and then examined their in situ signatures to find out if the CMEs impacted both spacecraft while STEREO-A moved closer to Wind from 60° to 20° in the longitudinal direction. They found that only four out of 21 CMEs impacted both spacecraft, suggesting an average CME angular width of around 30°. This

[1] https://www.affects-fp7.eu/helcats-database/database.php

angular width is smaller than the typical value of ∼60° found in past studies, in which an extreme case even showed a CME angular width of 110° (F. Carcaboso et al. 2024).

In this context, the present study aims to further investigate the angular width and properties of CMEs with angular separations at close distances through a comprehensive analysis of multipoint measurements from the STEREO-A spacecraft and spacecraft located at the first Lagrange point, L1, between 2022 January and 2023 August. During this period, STEREO-A covered angular separations from 35° to 0° relative to the Sun–Earth line. Combined with the increasing solar activity as solar cycle 25 approaches its peak, this time frame offers an ideal opportunity for simultaneous CME detections by both spacecraft. By leveraging this unique observational configuration, we study CME structures and contribute to a deeper understanding of their spatial and temporal evolution within the heliosphere. In this paper, Section 2 describes the data and methods used, followed by an overview of the database we constructed. Section 3 discusses the distribution of the database. Then, Section 4 presents three case studies, while Section 5 covers the various statistical analyses. Finally, Section 6 provides a discussion of the results and concludes with insights drawn from the findings.

2. Data and Methods

2.1. Data

In this study, we use measurements by Wind, ACE, and STEREO-A from 2022 January to 2023 August. All data are currently available on NASA/SPDF. Wind and ACE are in orbits at the L1 point at ∼0.98–0.99 au in heliocentric distance, and STEREO-A is orbiting the Sun at a heliocentric distance of 0.95–0.98 au and separating by ∼22° per year from the Sun–Earth line. During the period of this investigation, from 2022 January to 2023 August, the longitudinal separations between STEREO-A and spacecraft near L1 decreased from 35° to 0°. We use magnetic field data from the Magnetic Field Investigation (R. P. Lepping et al. 1995) and plasma parameters by the Solar Wind Experiment (D. Odstrcil & V. J. Pizzo 1999) from Wind, and In situ Measurements of Particles And CME Transients (M. H. Acuña et al. 2008) and the PLAsma and SupraThermal Ion Composition (A. B. Galvin et al. 2008) from STEREO-A (M. L. Kaiser et al. 2008). In this work, we use magnetic field and plasma data in an RTN coordinate system, where R is radially away from the Sun direction, N is parallel to the Sun's rotational axis, and T points to the vector product of the R and N directions. The data are resampled at a 1 minute resolution for Wind and STEREO-A and a 5 minute resolution for ACE. We use ACE for L1 measurements when there is an extended data gap from Wind.

2.2. CME Identification: Criteria and Database

We identified CMEs using the magnetic field and plasma data for individual spacecraft from 2022 January to 2023 August for STEREO-A and Wind. Some CMEs have a fast magnetosonic forward shock with a sharp increase in magnetic field, velocity, density, and temperature followed by a sheath region with a turbulent and compressed region of magnetic field and all plasma properties, but we do not require the presence of a shock or sheath to identify the MEs. The identification criteria for MEs are as follows: (i) enhanced magnetic field strength within the structure; (ii) a proton β (i.e., the ratio of proton thermal pressure to magnetic pressure) that is significantly below 1, typically at or below 0.1, but we did not use a strict quantitative criterion; and (iii) a duration of at least 12 hr. Smooth rotation and low variability in magnetic field components are expected in the ME part but are not mandatory. Additionally, proton temperature may be lower than the expected temperature ($T_{\rm exp}$), indicating unusual thermal properties within the CME (R. E. Lopez 1987), and a declining trend of the proton velocity profile is often found, suggesting CME expansion. After constructing our catalog, we compared our event identification and boundaries with the existing database of CMEs at L1 (I. G. Richardson & H. V. Cane 2010) and STEREO-A (HELCATS catalog; see C. Möstl et al. 2017). While we found a few differences, no modifications were made to our catalog based on these comparisons.

Based on the above identification criteria, we adopt the following method to determine if an ME is measured by both spacecraft. First, we examine the magnetic field components and plasma parameters to find a CME in each spacecraft individually. If a CME is detected at L1, we then check the data from the other spacecraft, STEREO-A, during the CME duration, with a window of ±10 hr, to look for similar CME signatures. We do so whether or not a CME was identified based on the set of criteria at STEREO-A. If both spacecraft show significant similarities in the trend of the parameters so that we are confident that a CME is measured at both spacecraft, the event is considered a "simultaneous event" (see Section 4.1). We repeat the same process starting from STEREO-A for further confirmation of the event identification done in the first step. If a simultaneous event is identified, we analyze the measurements from both spacecraft simultaneously to refine the boundary identification by identifying common features (e.g., discontinuities in the magnetic field measurements). Because a CME was measured at one spacecraft (e.g., at L1), the same time period at the second spacecraft (e.g., at STEREO-A) is analyzed with extreme care, and sometimes unclear CME or CME-like signatures can be identified.

When one spacecraft measures clear CME signatures but the other does not during the same period, this is labeled as a "single-spacecraft event." Other events, where the second spacecraft may detect some CME-like signatures but when those are not clear, are marked as "potential events" (e.g., see Section 4.2). We marked CMEs as "potential events" for various reasons: (i) when we found a clear CME at one spacecraft but unclear signatures at the other spacecraft; (ii) when the differences between the measurements at the two spacecraft are so large that we cannot be certain that they correspond to the same ME; (iii) when structures at both spacecraft do not have all clear characteristics of MEs but are not stream interaction regions (SIRs) or other corotating structures and the plasma and/or magnetic field measurements at the two spacecraft are somewhat similar; and (iv) when multiple team members do not agree on whether or not a specific time period corresponds to an ME at one of the spacecraft. We note that, for many of these potential events, there would be no CME identified if only single-spacecraft measurements were analyzed.

By visually inspecting data from STEREO-A, Wind, and ACE between 2022 January and 2023 August and applying the identification criteria discussed before, we compiled a database of 49 CME events, categorized into three groups. The first

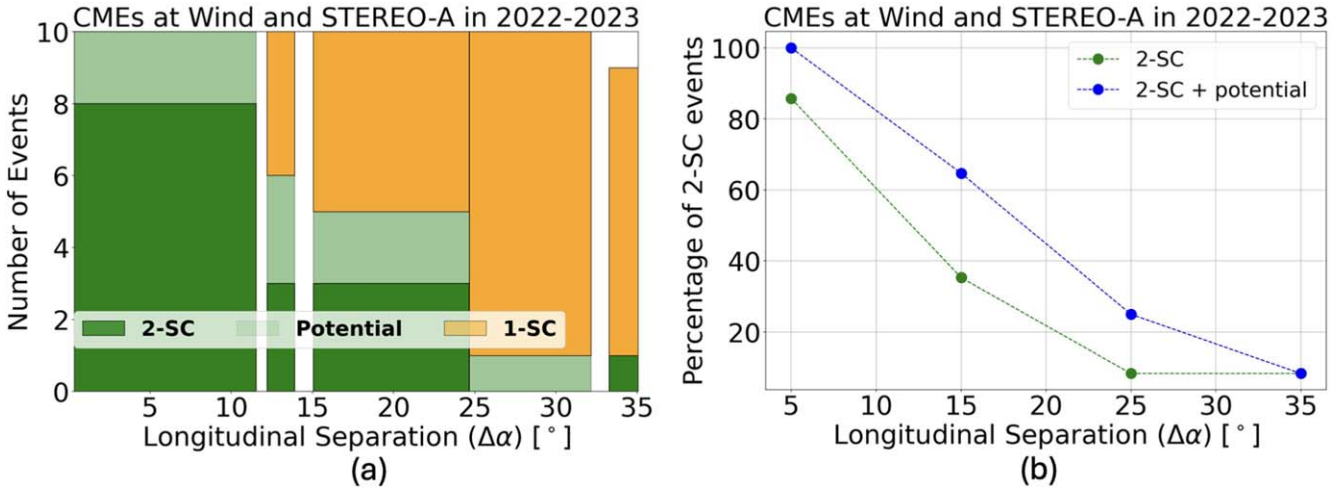

Figure 1. Panel (a) shows a histogram of all CMEs observed within the study period, binned by longitudinal separation ($\Delta\alpha$) into bins of 10 events, except for the last bin (nine events). Dark-green and light-green colors represent the counts of simultaneous (2-SC) and potentially simultaneous events, respectively, while yellow indicates single-spacecraft (1-SC) measurements within each bin. Panel (b) illustrates the variation in the percentage of simultaneous CMEs observed by both spacecraft as longitudinal separation increases. This percentage is calculated within each bin, with green points representing only 2-SC events and blue points including both 2-SC and potential simultaneous events.

group consists of 15 simultaneous events, in which both spacecraft detected clear ME signatures. The second group includes eight potentially simultaneous events, distributed across the four discussed categories: four events in category (i), two events in category (ii), and one event each in categories (iii) and (iv). The final group comprises 26 single-spacecraft events, with 10 observed exclusively by STEREO-A and 16 by Wind, each displaying clear CME signatures in one spacecraft but no detectable signs in the other.

Of the 72 spacecraft measurements analyzed, comprising 23 events that impacted both spacecraft (resulting in 46 measurements) and 26 events that impacted single spacecraft, 15 events are not recorded in either the HELCATS catalog (which has no plasma data updates after 2023 May) or the Richardson and Cane catalog.[2] However, these catalogs include 17 additional CMEs not listed in our data set. These discrepancies arise from two main factors: (1) some events we identify as a single CME are recorded as multiple CMEs in the catalogs, and (2) other structures we do not classify as CMEs are considered CMEs in the catalogs.

3. Database and Distribution of Multispacecraft CME Measurements with Longitudinal Separation

Using the 49 CMEs in our database, we investigate the distribution of simultaneous multispacecraft measurements with spacecraft longitudinal separation and its consequence for the angular width of CMEs. Figure 1(a) shows a stacked histogram of the longitudinal separations associated with CME measurements across three categories: confirmed simultaneous events (2-SC, dark green), potentially simultaneous events (potential, light green), and single-spacecraft measurements (1-SC, orange). The data set is divided into bins containing 10 events each, except for the last bin, which has nine events. This fixed bin size provides insight into the distribution of CMEs across different angular separations, with the bin widths varying based on the angular range with 10 events. This approach highlights angular ranges with higher or lower CME counts as a function of longitudinal separation angle. STEREO-A and Wind are both in the ecliptic plane and have a latitudinal separation that depends on the tilt of the ecliptic with respect to the solar equator.

From Figure 1(a), it is evident that simultaneous CME detections (2-SC events) become less frequent as the longitudinal separation between the two spacecraft grows, as expected. The first bin for separations of 0°–11° is the only one containing a majority of clear 2-SC events, but two CMEs were identified as potential simultaneous events due to insufficient similarities in their measurements. The following bin, covering separations from 12° to 14°, already contains four single-spacecraft events. As the separation increases further, especially between 15° and 25°, simultaneous observations decrease significantly, with only three out of the 10 CMEs in this range being 2-SC events. Beyond 25°, clear single-spacecraft (1-SC) measurements dominate, showing that larger longitudinal separations between the two spacecraft generally preclude simultaneous CME detection.

Additionally, we examine how the percentage of 2-SC events relative to the total number of events changes across the angular separation while binned in 10°. Figure 1(b) shows a clear trend: the percentage of simultaneous events declines rapidly with increasing separation. Specifically, at 15°, the percentage of 2-SC events (green dots) drops to 40%. The blue dots in the plot show that including potential events in the 2-SC category raises the overall percentage, but the limit at which 50% of events are measured by the two spacecraft, including potential events, is still around 20°.

We further investigate whether the inclination of the ME axis affects the simultaneous identification of CMEs. To examine this, we performed minimum variance analysis (MVA; B. U. Ö. Sonnerup & M. Scheible 1998) of the magnetic field for all 49 events to determine the inclination of the FRs axis. We found no correlation between the inclinations of the 2-SC, potential 2-SC, and 1-SC events. Therefore, there is no evidence of orientation dependency in the CME detection at the two spacecraft. We note that the ratio of eigenvalues was small for many of the events (for 18 measurements combining both spacecraft of 49 events, the ratio of intermediate to

[2] https://izw1.caltech.edu/ACE/ASC/DATA/level3/icmetable2.htm

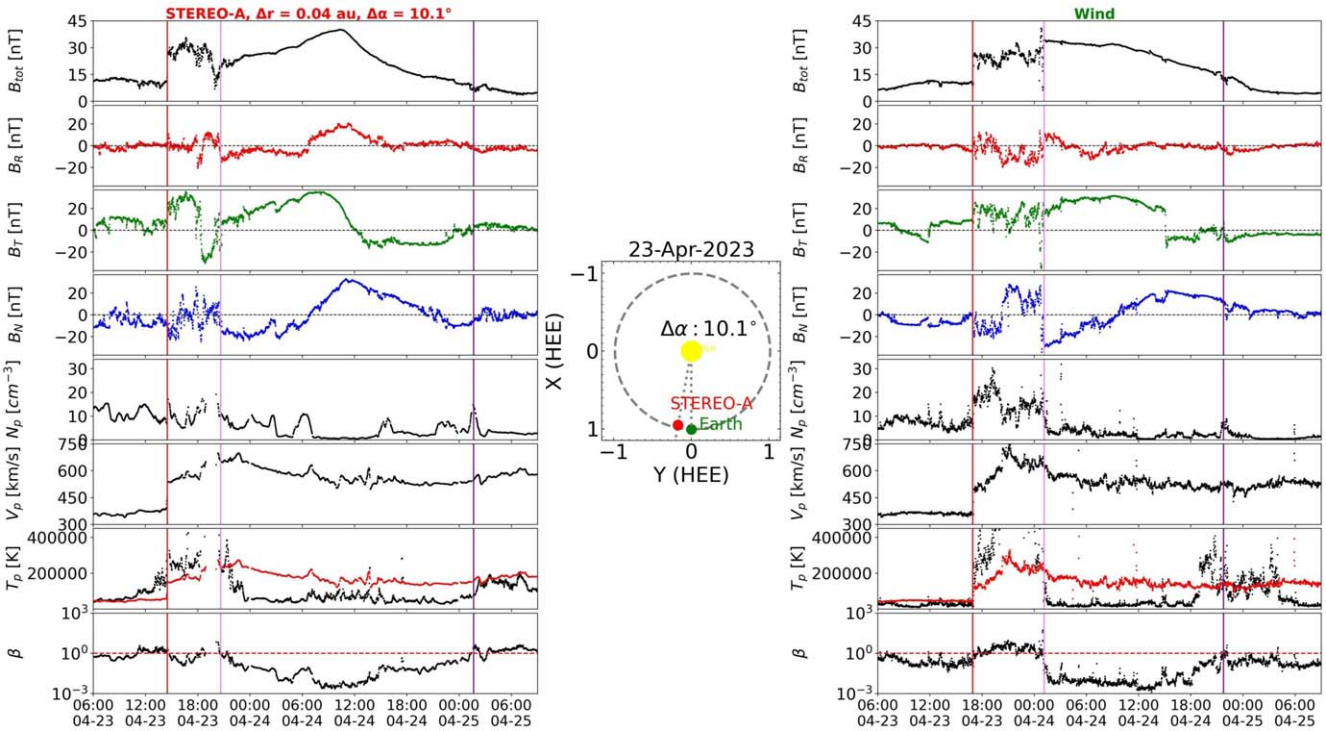

Figure 2. A CME on 2023 April 23, measured by Wind (right) and STEREO-A (left). The panels depict, from top to bottom, the total magnetic field and its components in RTN coordinates, the proton density, speed, and temperature (with the expected temperature in red), and proton β. Red, pink, and magenta lines denote the interplanetary shock and the start and end of the ME, respectively. The middle panel shows the position of the two spacecraft. An animated version containing all 49 CMEs in chronological order is available.

(An animation of this figure is available in the online article.)

Table 1
A Snippet of the Database of CMEs Measured by STEREO-A and L1 Spacecraft between 2022 January and 2023 August

Longitudinal Separation (deg)	Type	Spacecraft	Shock Time (UTC)	ME Start Time (UTC)	ME End Time (UTC)
10.1	2-SC	STEREO-A	2023-04-23 14:15:00	2023-04-23 20:37:00	2023-04-25 01:40:00
10.1	2-SC	L1	2023-04-23 16:44:00	2023-04-24 01:15:00	2023-04-24 21:46:00
10.4	Potential	STEREO-A	2023-04-20 01:56:00	2023-04-20 04:30:00	2023-04-20 15:30:00
11.0	Potential	L1	2023-04-18 13:26:00	2023-04-18 23:34:00	2023-04-21 05:08:00
13.9	1-SC	Wind	2022-12-18 19:40:00	2022-12-19 04:06:00	2022-12-20 08:08:00

(This table is available in its entirety in machine-readable form in the online article.)

minimum eigenvalues is <2), indicating that MVA was not reliable. This is consistent with the fact that many events were relatively weak and complex MEs, not MCs. We do not use the MVA results in the rest of the analysis. However, we were interested to see whether or not there is a correlation between orientation and 2-SC detection, as such a correlation is expected based on the traditional FR model with axial invariance. We further discuss the consequence of these measurements for the CME width in Section 6.

In summary, these results highlight the challenges of detecting CMEs simultaneously as the angular separation between spacecraft increases to even less than 35°, with the highest detection rates occurring at smaller separations (around 10°). The rapid decline in 2-SC detections as angular separation between two measurements increases highlights that CMEs may have a smaller angular size than suggested by previous studies. To improve our understanding of CME structure, more simultaneous CME measurements are needed, ideally with closely aligned spacecraft for more comprehensive CME studies.

4. Case Studies

In this section, we present examples of three types of CME measurements from our database that are identified as two-spacecraft, potential, and single-spacecraft events.

4.1. Simultaneous Two-spacecraft ME Measurements

On 2023 April 23, one CME was simultaneously (listed as type "2-SC" event in Table 1) measured by Wind and STEREO-A when they were separated by ∼10°.1 and ∼0°.9 in the longitudinal and latitudinal directions, respectively, and 0.04 au in the radial direction, as shown in the middle panel of Figure 2. The left panel in Figure 2 shows the in situ

measurements of the CME by STEREO-A. A fast forward shock distinguished by a sharp rise in magnetic field, velocity, and temperature was recorded at 14:35 UTC. The ME lasted 25.15 hr starting at 20:37 after a 6 hr long sheath region and ending at 1:45 UTC on April 25. The magnetic field inside the ME has smooth rotations in both B_T and B_N components, the magnetic field variability is decreased, and the magnetic field magnitude reaches its maximum near the middle of the ejecta. The mean magnetic field strength in the sheath and the ME are 26.1 nT and 24.3 nT, respectively. The velocity profile shows a decreasing trend in the first half of the ME and then becomes approximately constant. The entire CME propagates with a much higher speed than the solar wind before it. The average speed and expansion speed ($V_{\rm exp}$) are 577 km s^{-1} and 64 km s^{-1}, respectively. The $V_{\rm exp}$ is calculated as half of the speed difference between the 10 minute average speeds at the front and back of the ME. The ME region has a temperature that is significantly lower than the expected temperature of an expanding solar wind derived by R. E. Lopez (1987). The proton β is substantially below 1 inside the ME, indicating a magnetically dominated structure.

Wind measurements are shown in the right panel in Figure 2. A clear shock with a sharp increase in magnetic fields, number density, velocity, and temperature arrived at 16:54 UTC, i.e., ~2.5 hr later than at STEREO-A. The subsequent 8.52 hr of compressed and disturbed period corresponds to the sheath region between the shock and the ME. At 1:40 UTC on April 24, a discontinuity in all magnetic field and plasma parameters is observed and marked as the ME start time at 21:46 UTC on April 24. The ME of 20.51 hr duration is characterized by low variability in the magnetic field, smooth rotation in the north–south component of the magnetic field, cooler than expected temperature, a proton β that is significantly below 1, and the proton speed follows a similar trend as in STEREO-A (the slope of the speed profile found to be 3.7 km s^{-1} h^{-1} and 3.8 km s^{-1} h^{-1} at Wind and STEREO-A from the linear fit). The boundaries of the CME were chosen to be consistent for both spacecraft but not necessarily best suited for individual spacecraft. In this event, the ME start at Wind was identified by a clear southward turning of B_N, beginning with a low β and lower-than-expected temperature period. A similar discontinuity was observed at STEREO-A in B_T and B_N, although the temperature remained higher than expected. At the end of the low-β period, both spacecraft showed a spike in proton density and a drop in magnetic field magnitude, marking the ME end. While Wind experienced an earlier temperature increase, this time lacked clear magnetic field signatures that could be matched with STEREO-A. The mean speed and expansion speed at Wind are 532 km s^{-1} and 47 km s^{-1}, respectively. The peak in the total magnetic field occurs at the beginning of the ME. The mean magnetic fields at the sheath and ME are 24.8 nT and 26.8 nT, respectively.

This example highlights prominent CME signatures detected in both spacecraft. The total magnetic field strength is elevated compared to the ambient solar wind, although the overall field structure differs significantly between the two measurements. In STEREO-A, the east–west magnetic field component (B_T) exhibits a smooth rotation from east to west, whereas Wind data show a sharp discontinuity at ~15:06 UTC on April 24 in this component. Additionally, the sheath region at Wind lasted approximately 2 hr longer than the sheath observed at STEREO-A. Despite these differences, both spacecraft record a similar rotation in the north–south magnetic field component (B_N), which transitions from south to north. The proton velocity, temperature, and β profiles appear reasonably consistent between the two observation points. Based on the similarities between the measurements, the close arrival times at Wind and STEREO-A, and the longitudinal difference of only ~10° between the two spacecraft, this is clearly the same CME being measured simultaneously at the two spacecraft.

This event is particularly intriguing due to the combination of similarities and differences in the measurements at an angular separation of ~10°. Notably, the value of the distortion parameter (DiP), which is one of the proposed quantifications of the symmetry of the total magnetic field profile (T. Nieves-Chinchilla et al. 2018), is 0.42 at Wind and 0.44 at STEREO-A. This means both the magnetic field profiles are asymmetrically skewed toward the front, as the values at both measurements are less than 0.5. We also find the front-to-back ratio (F. Regnault et al. 2023) of the magnetic field strength of the ME is also remarkably similar at both spacecraft (2.12 at Wind and 2.14 at STEREO-A), despite the differing total magnetic field structures. The sheath-to-ME duration ratio is 0.21 at STEREO-A, but at Wind, it is exactly double, measuring 0.42; both are below the ~0.63 found earlier for 1 au events (M. Janvier et al. 2019). The CME exhibits some deviations from the simplest ME profiles at both locations. At STEREO-A, the B_N component shows a total rotation of more than 180° with a south-to-north-to-south rotation. At Wind, B_T undergoes a sharp discontinuity. It is unlikely that multiple FRs are present.

As noted, the shock arrived at STEREO-A approximately 2.4 hr earlier than at Wind. The expected travel time for a shock moving at ~536 km s^{-1} to cover the radial separation of 0.04 au between the two spacecraft is about 3 hr. For the ME front, with a speed of 651 km s^{-1}, it should have arrived at Wind in roughly 2.5 hr; however, the ME front was detected at Wind after 4.5 hr, indicating some inconsistency with the expected arrival time. It is possible that this inconsistency arises from the boundary selection (see the discussion above). While we prioritized the magnetic field, focusing on plasma parameters where the temperature decreases well below the expected temperature and the speed profile starts to decline monotonically would suggest shifting the end of the sheath at STEREO-A 1.5 hr later. This adjustment would make the sheath durations comparable (7.5 hr at STEREO-A and 8.5 hr at Wind) and align the expected ME front arrival with a 1 hr gap. As discussed above, we consider that the sheath boundaries that we chose are more likely to correspond to the true start of the ME as they correspond to clear changes in the magnetic field profile.

The density profiles at the two locations differ significantly. At STEREO-A, in the sheath region, the density is not very high, and within the ME, several density bumps are observed. In contrast, at Wind, the density is very high at the beginning of the sheath, then decreases slightly midway, and remains low throughout the ME.

We calculate the Pearson correlation coefficient between the two spacecraft measurements for the total magnetic field strength, its three components, and the proton bulk speed. We calculated the time lag between the measurements for the two spacecraft to maximize the correlation within the ME, similar to N. Lugaz et al. (2018). We do so separately for the total magnetic field strength and each of the components. Using the "best lag" time that yielded the highest correlation, we shifted

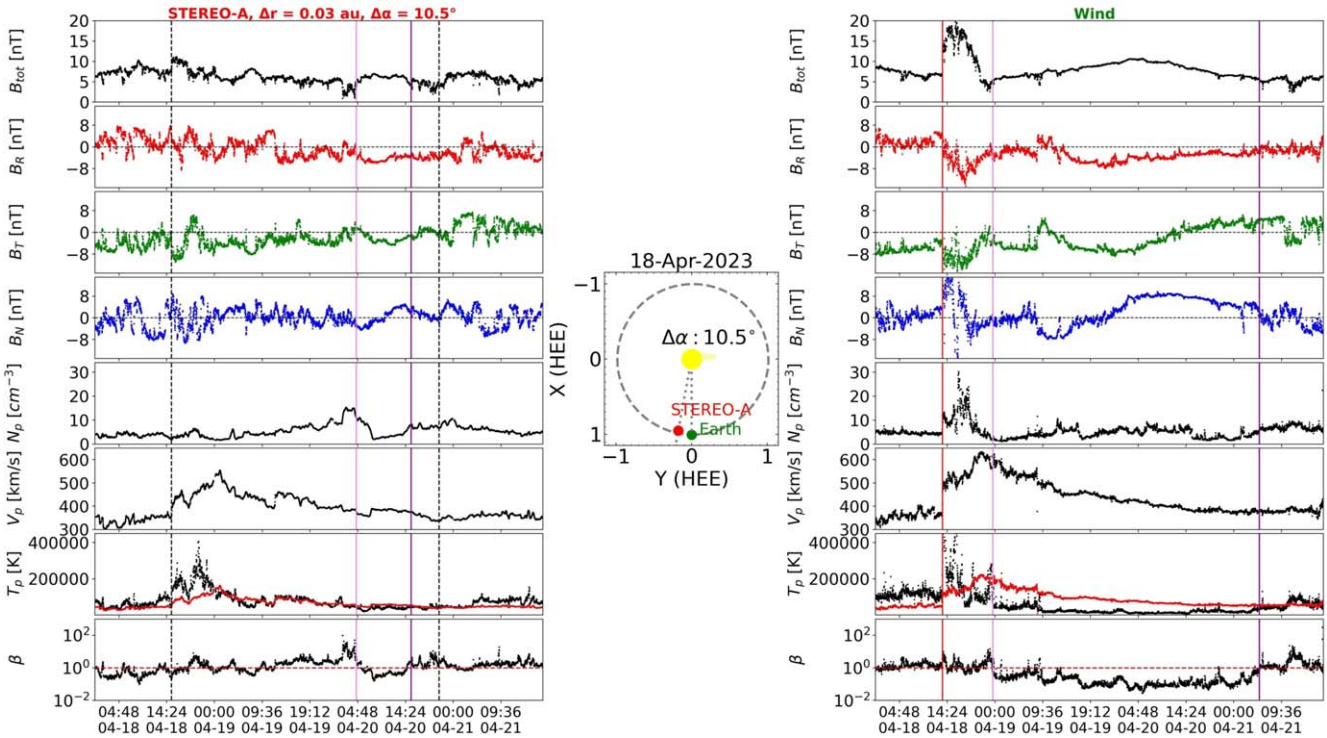

Figure 3. A CME is measured by Wind on 2023 April 18 and by STEREO-A on 2023 April 20. The panels are the same as described in the caption of Figure 2. On the left panel, two vertical black dashed lines are at the boundary within which V_p and T_p show similar trends to Wind.

the STEREO-A data and rebinned both Wind and STEREO-A data into 15 minute averages to compute the final correlation presented. For this event, the best lag is 141 minutes, which would correspond to a propagation speed of $\sim$566 km s^{-1} based on the STEREO-A–L1 difference in heliocentric distance. This is similar to the actual CME average speed. The maximum correlation of 0.92 was found for B_T, followed by 0.79 for V_p, and 0.77 for both $B_{\rm tot}$ and B_N. The lowest correlation coefficient was 0.32 for B_R. The potential reason for this is that B_R is close to zero on both spacecraft, so fluctuations around zero may result in a lower correlation. The rms error (RMSE) between the two spacecraft measurements is also calculated for this event using the 15 minute resolution data and best lag obtained earlier. The RMSEs found for $B_{\rm total}$, B_R, B_T, B_N, and V_p are 6.13 nT, 8.76 nT, 7.45 nT, 9.77 nT, and 45.6 km s^{-1}. As percentages of the maximum magnetic field, these are 14%, 22%, 20%, and 27%, and for proton speed, 6%.

An effort to model the distorted cross-sectional shape and deformed ME axis of this event was made by A. J. Weiss et al. (2024), who claimed to have successfully reconstructed the individual observations and provided a reasonable reconstruction for the multispacecraft data. However, their selection of boundaries differs significantly from ours. A significant portion of the front ME in STEREO-A and the back ME in Wind were not considered in their analysis, which is crucial and may affect the accuracy of the reconstruction or fitting of the event. Their work indicates that, to understand these measurements, it is necessary to go beyond the assumptions of a straight axis, which is a conclusion we share.

4.2. A Potential Simultaneous Event

In Figure 3, the panels show the time profile of the "potential" event listed in Table 1: STEREO-A in situ measurements, the spacecraft's orbit in the ecliptic plane, and Wind measurements, from left to right, respectively. Wind measured a clear CME characterized by a shock at 13:26 UTC on 2023 April 18, a sheath region of $\sim$10 hr, and an ME exhibiting an enhanced magnetic field from 23:34 UTC on 2023 April 18 to 5:08 UTC on 2023 April 21. In the ME, there was a rotation in the north–south component of the magnetic field (B_N), accompanied by a decreasing velocity profile, colder than expected proton temperatures, and a low β profile. In contrast, within $\sim$10° separation, we identified a potential and short ME without shock in front at 4:30 UTC that ended at 15:30 on April 20 in STEREO-A characterized by relatively weak β and smoother but relatively weak magnetic fields. Without the simultaneous Wind measurements to guide us to look for a CME during this time period, no CME would have been identified. STEREO-A detected a structure with a significantly shorter duration, lacking a sheath region, a weaker magnetic field strength, and showing only minimal rotation in the B_N component. The recorded temperatures were similar to the surrounding solar wind, and the β value profile remained low.

As discussed in Section 2.2, the two spacecraft data are not prominent enough to be considered simultaneous events but are somewhat similar, so we consider them as a potential event, in this case, because the period identified at STEREO-A can only be classified as a potential ME. If this is truly a simultaneous event, at 10° separation, the duration of the event is very different, and it would be a very glancing encounter at STEREO-A. One CME of that kind is presented here. Interestingly, the velocity and temperature profiles closely resembled those measured by Wind throughout the entire observation period. The magnetic field components in STEREO-A displayed a similar trend but over a much shorter duration than the magnetic field components within the ME

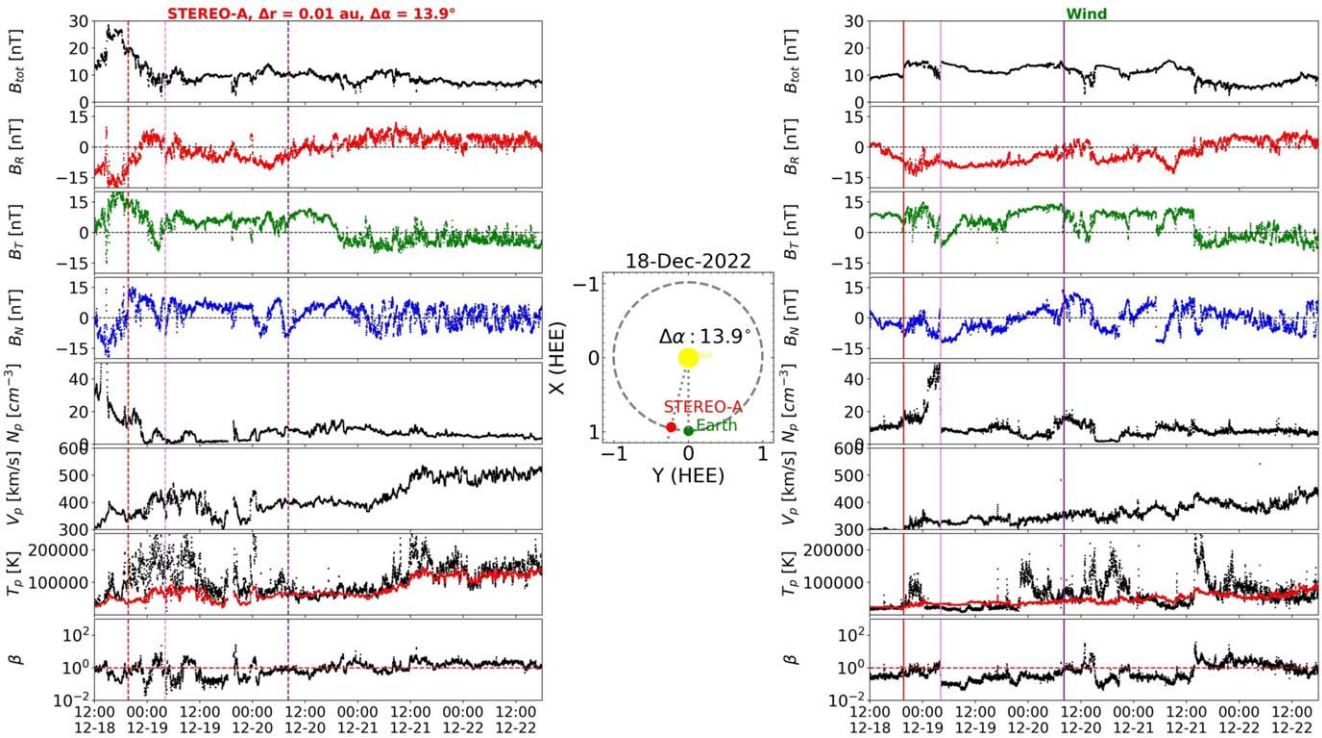

Figure 4. On 2022 December 18, a CME was measured by Wind while STEREO-A was separated by 13.°9 in the longitudinal direction, and radial separation was 0.01 au. The panels exhibit the same as Figure 2. The vertical dashed lines represent the corresponding times for the shock, ME start, and end time at Wind.

observed by Wind. It is not clearly understood why these notably similar yet different features were observed by the two spacecraft within such proximity.

The mean magnetic field strengths recorded at STEREO-A and Wind are 5.9 nT and 7.8 nT, respectively. These are comparable to the magnetic field strength before the event, but the CME exhibits additional plasma signatures, including low β, as described below. At Wind, the CME exhibits an expansion velocity of 104 km s^{-1}, while no noticeable expansion is observed at STEREO-A using the boundaries of the potential ME, but a decreasing speed profile with an "expansion" of $\sim$112 km s^{-1} can be seen using the Wind ME boundaries at STEREO-A. The average bulk speeds are 377 km s^{-1} at STEREO-A and 439 km s^{-1} at Wind. Interestingly, despite these differences in speed and expansion, the DiP of the ME is similar at both locations, with values of 0.50 at STEREO-A and 0.51 at Wind. We have done the correlation and RMSE study on potential events too. For this event, we consider the black dashed and solid magenta lines as boundaries for these analyses, as the speed has a similar trend as Wind for this time period. Additionally, since the ME durations differ significantly between the two spacecraft, calculating the correlation using only the shorter STEREO-A duration would be misleading, as it would capture only a small segment of the Wind ME rather than the entire structure. Using these boundaries, we found the best lag to be −398 minutes, and the highest correlation of 0.89 was obtained in proton speed as expected. For the total magnetic field and for B_R, B_T, and B_N, the correlation coefficients are found to be −0.30, 0.24, 0.56, and 0.40. The RMSEs for $B_{\rm total}$, B_R, B_T, B_N, and V_p are 3.21 nT, 2.76 nT, 3.88 nT, 5.72 nT, and 45.02 km s^{-1}. The $B_{\rm tot}$, R, T, and N components as percentages of the maximum magnetic field were 31%, 29%, 31%, and 46%, and for proton speed, we found the RMSE value to be 11% as a percentage of maximum proton speed.

4.3. A Single-spacecraft Event

At an angular separation of approximately 14°, as shown in Figure 4, Wind observed a clear CME starting with an enhanced magnetic field that ended on 2022 December 20 at 8:08 UTC. The sheath region exhibited increased magnetic field strength, density, and temperature. Within the ME, the B_N component showed a partial rotation from south to north, accompanied by a low proton β profile. Most of the ejecta remained cooler, except for the final portion, where the temperature increased. However, the bulk proton speed did not display the typical decreasing trend within the ME and instead had a relatively flat profile.

In contrast, STEREO-A recorded significantly different magnetic field and plasma conditions. None of the magnetic field components showed any rotation, the proton temperature was highly elevated and more disturbed compared to the background, and the proton β exhibited multiple sharp discontinuities. Although the proton speed at STEREO-A was higher than at Wind, it showed no clear trend of decrease. Based on our identification criteria, there were insufficient signatures in the STEREO-A data to classify this event as a CME. At STEREO-A, a rotation in B_T and B_N is observed approximately 24 hr after the CME arrived at Wind. However, given the previously discussed differences in the magnetic field and plasma measurements, the absence of overlapping features between the two spacecraft, and the fact that STEREO-A, positioned 0.01 au ahead of Wind, would logically observe the CME first, we conclude that STEREO-A did not record the same CME as Wind. The average values for the magnetic field, proton speed, and expansion speed within the ejecta period are

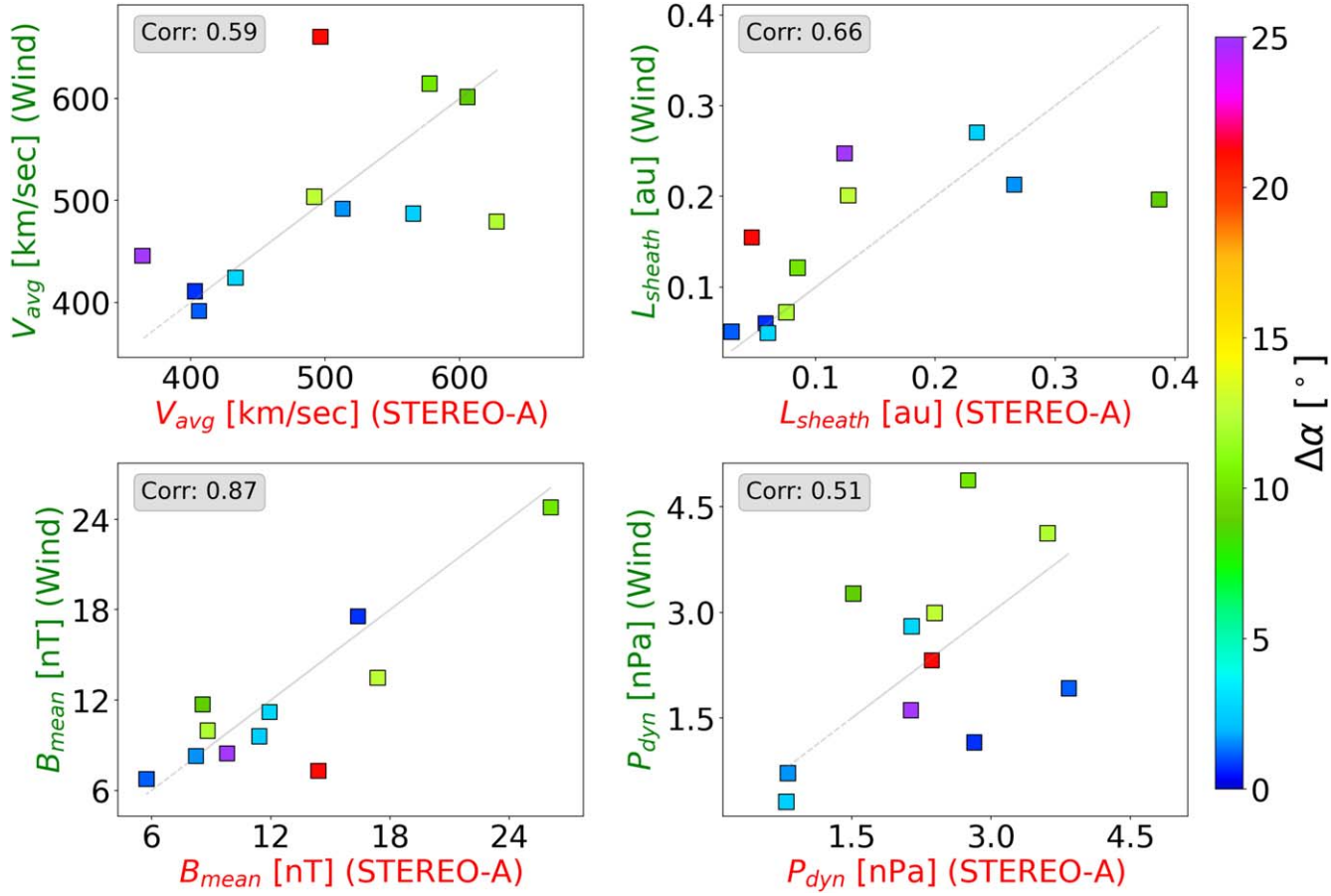

Figure 5. Various sheath properties at one spacecraft are plotted against the corresponding measurements from the other spacecraft. The top panels display the mean speed and sheath length, while the bottom panels show the mean magnetic field and dynamic pressure for each simultaneous CME. The symbols are color coded by the longitudinal separation between the two spacecraft, as indicated on the right-hand side color bar.

10 nT, 422 km s^{-1}, and 13 km s^{-1} at STEREO-A, and 10 nT, 366 km s^{-1}, and 15 km s^{-1} at Wind, respectively, for the corresponding ME region. The measurements at STEREO-A are consistent with a small stream interaction region (simultaneous increase in the density and magnetic field strength). This is consistent with an HSS with a velocity of 500 km s^{-1} measured at STEREO-A starting on December 21 at STEREO-A and on December 23 at Wind. Small CMEs are often embedded within SIRs, which might be what is observed at Wind here (A. P. Rouillard et al. 2010).

5. Statistical Analysis

With the 15 confirmed 2-SC events and eight potential ones, we can perform some statistical studies to find out which CME properties are most consistent between the two spacecraft, both for the ME and the sheath. We further analyze the properties of the sheaths and MEs for 14 simultaneous CMEs measured by the two spacecraft with varying angular separation.

5.1. Sheath Properties

Figure 5 presents the sheath properties, including average velocity, sheath length, mean magnetic field, and dynamic pressure, as measured by the two spacecraft. Out of the 15 two-spacecraft CMEs, one event (on 2022 November 11 when $\Delta\alpha$ was 15.°1) lacks a sheath at both spacecraft. Additionally, the Wind spacecraft does not detect a sheath for two more events (2022 October 21 and 2022 December 26, corresponding to separations of 16.°2 and 14.°0), while STEREO-A does not measure a sheath for another event on 2023 January 3, corresponding to a separation of 13.°8. As a result, there are four CMEs without corresponding 2-SC sheath measurements, leaving only 11 data points in Figure 5 for comparison. The length ($L_{\rm sheath}$) is calculated by multiplying the mean proton speed by the sheath duration. The dynamic pressure is determined by multiplying the mean proton density by the square of the mean proton speed.

The four sheath properties plotted in Figure 5 show a moderate-to-strong correlation between the two spacecraft. This is especially true for the mean magnetic field strength (bottom left), which remains relatively consistent between the two spacecraft, with data points for closely separated events (blue) clustering near the $y = x$ line and with even points for separations of 10°–15° (green points) remaining close to the $y = x$ line. In contrast, red and purple points, representing larger separations, tend to deviate more significantly. While various plasma and magnetic field parameters such as duration, length, and magnetic field strength are shown, only a few exhibit a clear trend with longitudinal separation, suggesting that, for this limited sample size, the sheath properties are not strongly affected by the angular separation, as long as both spacecraft measure a sheath. We note that all nine events measured by the two spacecraft for separations of less than 13° have a sheath at both spacecraft but only two out of the six events with larger separations. N. Lugaz et al. (2022) analyzed in detail one event

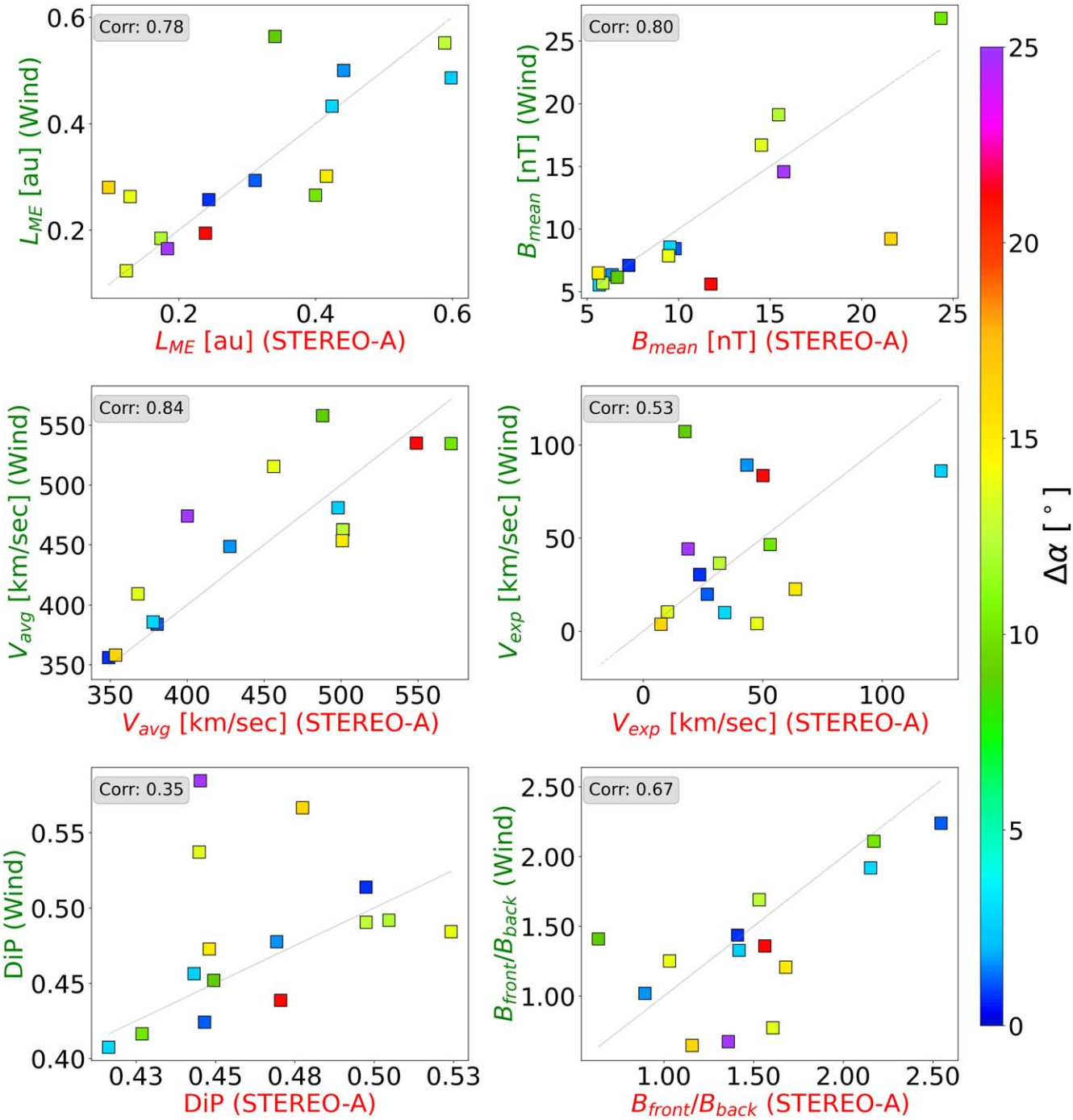

Figure 6. Properties of all 15 MEs associated with multispacecraft measurements within our observation period, with each symbol color coded with the spacecraft angular separation, as shown by the right-hand side legend.

for separations of 55° with a sheath at STEREO-A but not at Wind.

5.2. ME Average Properties

Next, we study the properties of the MEs similarly to the sheath. Here, we include other parameters, such as the DiP and front-to-back ratio of the magnetic field strength (F. Regnault et al. 2023) along with various plasma and magnetic field-related parameters, such as length ($L_{\rm ME}$), magnetic field strength ($B_{\rm mean}$), expansion velocity ($V_{\rm exp}$), and average velocity ($V_{\rm avg}$). Figure 6 shows that the mean magnetic field and average velocity are strongly correlated between both spacecraft measurements, with a correlation coefficient (corr. coeff.) of 0.8 for $B_{\rm mean}$ and 0.84 for $V_{\rm avg}$. The length (corr. coeff.: 0.78), expansion speed (corr. coeff.: 0.53), and front-to-back ratio of $B_{\rm tot}$ (corr. coeff.: 0.67) are moderately consistent.

Of the three different ways to quantify the ME expansion, the front-to-back ratio of the magnetic field strength is the one with the highest correlation between the measurements at the two spacecraft. The DiP has a small standard deviation of 0.04 around the median of 0.47 but no clear correlation between the

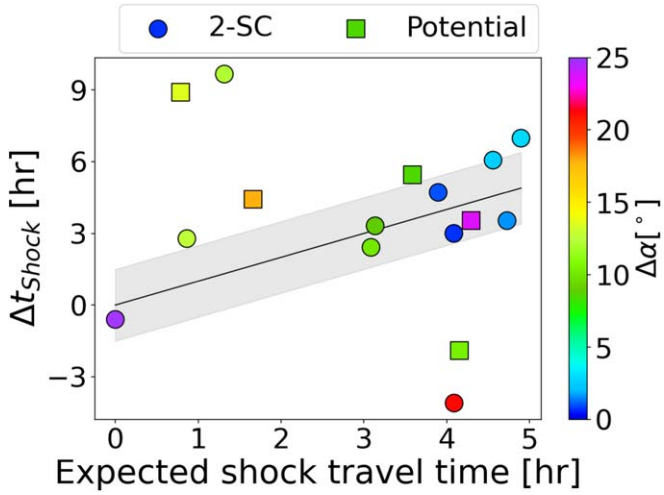

Figure 7. Shock transit time, measured vs. expected. The color bar shows the longitudinal separation associated with each CME. The circles and squares represent the 2-SC and potential 2-SC events. The shaded region is within ±1.5 hr from the $y = x$ line, which is shown by the black line. See the text for details on the calculations.

measurements. The expansion speed shows clustering around 30–60 km s^{-1}. Note that all these ways of quantifying the expansion are affected by the choice of boundaries.

5.3. Delay in Shock Arrival Time between the Two Spacecraft

Additionally, we examine the shock travel time between the two spacecraft for both 2-SC as well as potential 2-SC events. Sixteen events have a shock at both spacecraft, including 11 out of the 15 2-SC events and five out of the eight potential events. Figure 7 shows the deviation between the measured difference in shock arrival times at the two spacecraft from the expected shock arrival time at one spacecraft, as inferred from the other. To calculate the expected shock arrival time, we used the separation in radial distance between STEREO-A and Wind/ACE, along with the shock speed measured by STEREO-A (averaged over 30 minutes following the shock). Excluding four events measured at an angular separation of approximately 10°–20°, the shock arrival times generally show consistent agreement (within the gray area, which is ±1.5 hr deviated from the $y = x$ line). This suggests a general consistency in shock propagation between the two points, except 4–6 events (approximately 20%–30% of total events) that showed variability in shock arrival times.

Four events deviate significantly from the general pattern. Two of these are 2-SC events: one on 2023 March 22, detected when the spacecraft were approximately 12° apart, and another on 2022 August 18, detected at an angular separation of ∼21°. For the March event, the shock speed at STEREO-A was about 650 km s^{-1}, suggesting it would reach Wind in roughly 1 hr. However, the shock speed recorded at Wind was much lower, ∼500 km s^{-1}, resulting in a delay of over 9 hr. Additionally, two potential 2-SC events occurred on 2023 April 18, with a separation angle of $\Delta\alpha = 11^\circ$ where STEREO-A did not record a clear shock but some sort of disturbances near the black dashed line (see Figure 3), although Wind has a clear shock. Another is on 2023 February 20, when $\Delta\alpha = 13^\circ$. For the February event, the expected shock travel time difference was about 1 hr, but it took over 9 hr for the shock detected at STEREO-A to reach Wind. This indicates that the shock or shock-like disturbances associated with these events are propagating nonradially. Additionally, for significant longitudinal separations, the shape of the CME and the specific part that impacts the other spacecraft could influence the shock arrival timing, resulting in the observed behavior.

5.4. Detailed Comparison of the Measurements between the Two Spacecraft

We calculate the Pearson correlation coefficient for the magnetic field components and the total magnetic field for the 15 simultaneous 2-SC and eight potential simultaneous events using time-series data from STEREO-A, Wind, and ACE following N. Lugaz et al. (2018). Figure 8 presents the correlation trends for $B_{\rm tot}$, B_R, B_T, B_N, and V_p with increasing longitudinal separation between STEREO-A and the L1 spacecraft. To account for the different CME arrival times at the two spacecraft, we shift one spacecraft's data before calculating the Pearson correlation. The optimal time for shifting the data is determined by maximizing the correlation in the total and individual magnetic field components, with the shift time varying between −500 and 500 minutes. The best shift corresponds to the one that yields the maximum correlation in any component in 1 minute resolution. We then apply this best lag to shift the data for all parameters ($B_{\rm tot}$, B_R, B_T, B_N, and V_p) and compute the correlation coefficients using the 15 minute average of the data.

Figure 8 illustrates how the correlation coefficients vary with increasing angular separation between the two spacecraft. The correlation for the magnetic field components is mostly below the moderate correlation threshold (0.5), but only eight and nine events are below that line for V_p and $B_{\rm tot}$, respectively. Although the correlation coefficients for the magnetic field components decline sharply with separation, $B_{\rm tot}$ maintains higher values up to an angular separation of 20° with significant scatter. The figure indicates that, on average, the correlation for the total magnetic field approaches zero when the separation between the two spacecraft reaches 15°–25°, while it reaches zero closer to 10° for the magnetic field components.

To further examine the consistency in the trends of various CME properties between the two spacecraft, we analyze the RMSE of magnetic field and speed measurements at both locations. We use data over the entire ME duration after incorporating the best lag time for each event (as discussed earlier) to calculate the RMSE. The values are normalized to the maximum magnetic field strength for $B_{\rm tot}$, B_R, B_T, and B_N and by the maximum velocity for V_p. We use the maximum at whichever spacecraft has the maximum value for this particular parameter. These RMSE values may serve as a quantitative measure of global-scale similarities. We find moderate correlations between the RMSEs and the angular separation. While there is significant scatter around a trend of increasing values for increasing separations, the scatter is less than for the correlation coefficient, as presented above. The slope of increase appears highest for B_T, B_N, and $B_{\rm tot}$ and lowest for V_p, as shown in Figure 9.

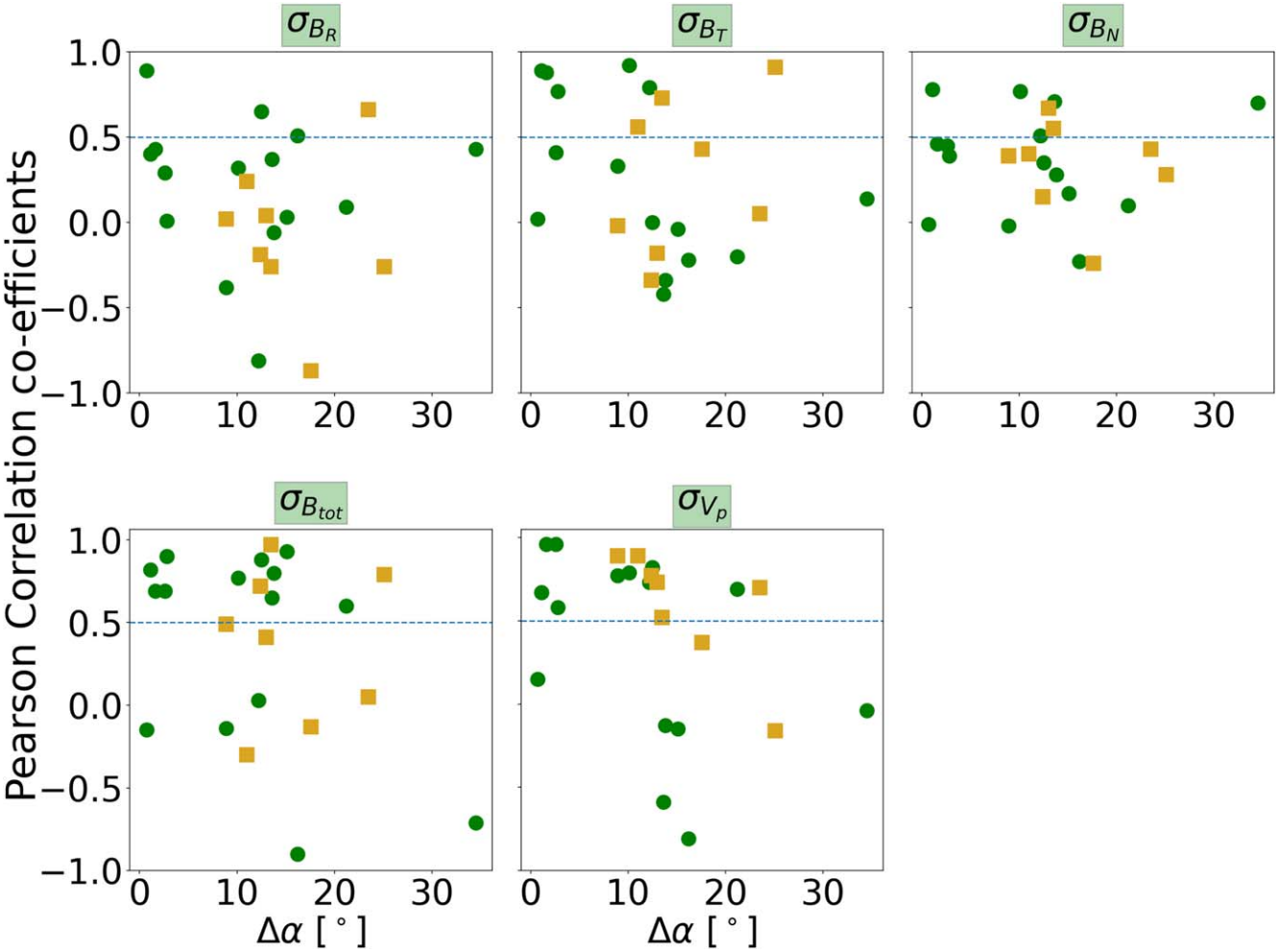

Figure 8. Pearson correlation between Wind and STEREO-A measurements. The top panel displays variations in correlations for the B_R, B_T, and B_N components across longitudinal separations, while the bottom panel shows the correlation for the total magnetic field and proton bulk speed. 2-SC events are shown with green circles and potential events with yellow squares. The blue dashed line indicates a moderate correlation, with a value of 0.5.

6. Discussion and Conclusions

In this study, we build a catalog of CMEs measured by spacecraft at L1 (Wind and/or ACE) and the STEREO-A spacecraft at a time when their longitudinal separation varied from 35° to 0°, spanning the period from 2022 January to 2023 August.

Of the 49 CMEs detected at either spacecraft, only 15 were clearly recorded by both spacecraft. Ideally, one would expect all CMEs within 25°–35° of the Sun–Earth line to have a high possibility of impacting both spacecraft, as past research based on remote observation suggests CME angular widths range from 47° to 61° based on remote-sensing images (S. Yashiro et al. 2004) and ∼30° to 60° based on in situ measurements (H. V. Cane et al. 1997; S. W. Good & R. J. Forsyth 2016; N. Lugaz et al. 2024a). Our analysis, shown in Figure 1, reveals that 31% of all CMEs were observed by both Wind and STEREO-A. When "potential" simultaneous events are included, this percentage rises to 47%. Within a separation of approximately 12°, 70%–100% of CMEs were recorded by both spacecraft, but this drops to 30% for separations greater than 12° up to 25°. This suggests that the average angular full width of CMEs in our data set falls between 25° and 40°. This finding aligns with another recent study by N. Lugaz et al. (2024a), which investigates the angular width of MEs within CMEs using data from STEREO-A and L1 for CMEs propagating within 30° of both STEREO-A and L1 spacecraft. Taken together, these results suggest that the angular width of MEs at 1 au is ∼30°, or about twice narrower than previously assumed. Nevertheless, some CMEs may exhibit exceptionally large angular widths with two-spacecraft measurements reported up to 110° (see, e.g., F. Carcaboso et al. 2024). However, besides that event, the largest reported two-spacecraft measurements of MEs at similar heliocentric distances are 55° (N. Lugaz et al. 2022) and 41° (C. J. Farrugia et al. 2011) for STEREO and ∼55°–60° for Helios (H. V. Cane et al. 1997; V. Bothmer & R. Schwenn 1998). This indicates that, except in extremely rare cases, the maximum ME longitudinal extent may be only ∼50°–60°.

Further, we analyze the properties of the ME and CME sheaths recorded simultaneously by both spacecraft. Our analysis reveals that, while there is substantial variability in individual CME profiles across different events, several global characteristics, especially the average magnetic field strength and proton speed, remain consistent for both the sheath and ejecta regions between the two spacecraft. We also find that this is not true for the ME expansion speed and DiP, two parameters often used to quantify CME expansion. We find that the front-to-back ratio of

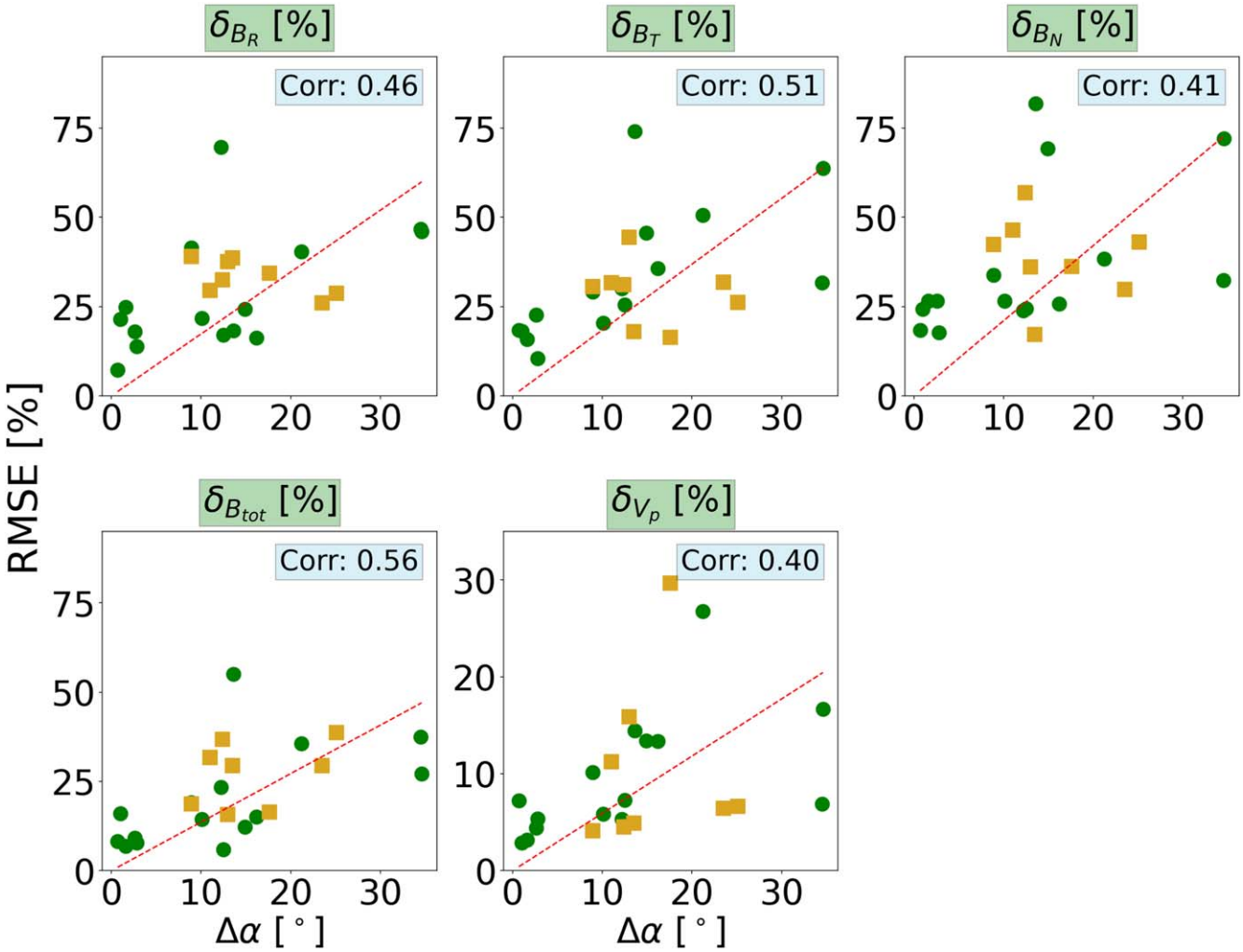

Figure 9. The RMSE percentages between Wind and STEREO-A measurements are shown. The organization and symbols are the same as in Figure 8. The red dashed line is the least square fitting to the data.

the magnetic field, as used in F. Regnault et al. (2023), is the most consistent measure of the CME expansion between the two spacecraft. To further quantify these similarities and differences in trend, we computed the Pearson correlation and RMSE for the magnetic field and proton speed time series between the two spacecraft. The results show that the correlation decreases with increasing angular separation from 0° to 35° with very large variability between different events. The total magnetic field ($B_{\rm tot}$) and proton speed (V_p) display the highest correlation to large separations.

The RMSE between the two satellite measurements is found to show a clearer trend with angular separation. This suggests that, for moderate to large angular separations such as in our case, the RMSE serves as a more reliable metric than correlation for assessing the similarities of CME profiles at different locations. For the magnitude of the magnetic field ($B_{\rm tot}$), the RMSE is similar for the potential events compared to the confirmed 2-SC events; no firm conclusions can be made for the velocity and the magnetic field components either. A larger number of events will provide a clearer understanding of how the correlations vary with angular separation and how potential events differ from confirmed ones.

We investigate the curvature or tilt of CME-driven shock fronts by analyzing the 16 events with shocks or shock-like disturbances ahead of the ME. Our analysis reveals that, for most cases, the measured travel times between STEREO-A and L1 align closely with the expected values based on the speed measured at STEREO-A, with deviations within ±1.5 hr. A recent study by F. Regnault et al. (2024) found a delay of −2 hr in shock arrival while the expected time was 5.5 hr, similar to that observed in one of our outliers (marked by a square in the lower-left corner of Figure 7). Events with significant deviations from expected travel times may result from local interactions with the IMF or solar wind, shock dimples, or shock tilts (M. Neugebauer & J. Giacalone 2005; A. Szabo et al. 2010). Overall, our findings indicate that the CME-driven shock front, in most cases, is largely spherical and propagates primarily in a radial direction. This suggests that a sentinel-like spacecraft, like STEREO-A between 2023 April and 2024 December, can be used to predict shock arrivals at L1 (R. Laker et al. 2024). However, a larger sample size is needed to confirm this with greater confidence and to investigate the shock radius of curvature from multispacecraft measurements.

Overall, this study sheds some light on the nature of MEs. They are narrower than previously thought, and the average speed and magnetic field strength are nearly equal throughout the ME, indicating that MEs are indeed global coherent structures, at least on scales of 10°–20°, confirming results

from more than 40 yr ago (L. Burlaga et al. 1981). However, the magnetic field components have very little correlation for most CMEs, even for separations of 5°–15°. This is hard to reconcile with the paradigm of MEs as twisted FRs with straight axes and axial invariance. If confirmed, such studies should be used to refine our theoretical models of MEs (N. Al-Haddad & N. Lugaz 2025), to validate large-scale numerical simulations of CMEs, and to further investigate CME coherence, as done theoretically by M. J. Owens (2020) and through simultaneous measurements at close separation in C. Scolini et al. (2024).

The potential CME events follow similar correlation and RMSE trends for magnetic field and proton speed as the 2-SC events. This may indicate that such events are indeed simultaneous events, though identifying these potential events was challenging due to significant differences in the measurements. This suggests the need for a more objective method to identify CMEs than is currently used (S. Pal et al. 2024).

In the future, we plan to expand the database of simultaneous 2-SC CME events as STEREO-A continues to move past the Sun–Earth line, reaching angular separations of up to 35° from the Sun–Earth line at the end of 2024, when solar activity is expected to peak. During the current study period, which was near the solar maximum but not yet at its peak, we observed a relatively high number of CMEs (49 over 20 months). There were, however, no instances of CME–CME interactions to complicate the analysis of individual CME properties, unlike the complex events analyzed by Y. D. Liu et al. (2024). We expect the investigation of the end of 2023 and 2024 to be significantly more complicated due to the larger number of such complex events. However, the CME data from 2023 to 2024 as measured by STEREO-A and L1 shall provide an order of magnitude more simultaneous events than were measured by STEREO-A, STEREO-B, and L1 in the first 1.5 yr after launch (E. K. J. Kilpua et al. 2011b). This will enable us to further investigate the size, morphology, and properties of CMEs.

Acknowledgments

We are grateful to the PDS archive (https://cdaweb.gsfc.nasa.gov/) for providing the data distribution for ACE, Wind, and STEREO-A data. S.A.B. and N.L. acknowledge support from 80NSSC20K0700, 80NSSC24K1245, and 80NSSC20K0431. N.A. acknowledges support from 80NSSC21K0463. C.J.F. acknowledges support from NASA grant 80NSSC19K1293. B. Z. acknowledges the NASA ECIP grant 80NSSC23K1057 and the NSF grant AGS-2301382.

ORCID iDs

Sahanaj A. Banu https://orcid.org/0009-0001-4878-9157
Noé Lugaz https://orcid.org/0000-0002-1890-6156
Bin Zhuang https://orcid.org/0000-0002-5996-0693
Nada Al-Haddad https://orcid.org/0000-0002-0973-2027
Charles J. Farrugia https://orcid.org/0000-0001-8780-0673
Antoinette B. Galvin https://orcid.org/0000-0003-3752-5700sahanaj.banu@unh.edu

References

Acuña, M. H., Curtis, D., Scheifele, J. L., et al. 2008, SSRv, 136, 203
Al-Haddad, N., & Lugaz, N. 2025, SSRv, 221, 12
Ala-Lahti, M., Ruohotie, J., Good, S., Kilpua, E. K. J., & Lugaz, N. 2020, JGRA, 125, e2020JA028002
Bothmer, V., & Schwenn, R. 1998, AnGeo, 16, 1
Burlaga, L., Sittler, E., Mariani, F., & Schwenn, R. 1981, JGR, 86, 6673
Byrne, J. P., Maloney, S. A., McAteer, R. T. J., Refojo, J. M., & Gallagher, P. T. 2010, NatCo, 1, 74
Cane, H. V., Richardson, I. G., & St Cyr, O. C. 1998, GeoRL, 25, 2517
Cane, H. V., Richardson, I. G., & Wibberenz, G. 1997, JGR, 102, 7075
Carcaboso, F., Dumbović, M., Kay, C., et al. 2024, A&A, 684, A90
Farrugia, C. J., Berdichevsky, D. B., Möstl, C., et al. 2011, JASTP, 73 1254
Galvin, A. B., Kistler, L. M., Popecki, M. A., et al. 2008, SSRv, 136, 437
Good, S. W., & Forsyth, R. J. 2016, SoPh, 291, 239
Good, S. W., Forsyth, R. J., Raines, J. M., et al. 2015, ApJ, 807, 177
Gosling, J. T. 1990, GMS, 58, 343
Howard, T. A., & DeForest, C. E. 2012, ApJ, 746, 64
Janvier, M., Winslow, R. M., Good, S., et al. 2019, JGRA, 124, 812
Jian, L. K., Russell, C. T., Luhmann, J. G., & Galvin, A. B. 2018, ApJ, 855, 114
Kaiser, M. L., Kucera, T. A., Davila, J. M., et al. 2008, SSRv, 136, 5
Kay, C., Opher, M., & Evans, R. M. 2015, ApJ, 805, 168
Kilpua, E., Koskinen, H. E. J., & Pulkkinen, T. I. 2017, LRSP, 14, 5
Kilpua, E. K. J., Jian, L. K., Li, Y., Luhmann, J. G., & Russell, C. T. 2011a, JASTP, 73, 1228
Kilpua, E. K. J., Lee, C. O., Luhmann, J. G., & Li, Y. 2011b, AnGeo, 29, 1455
Kilpua, E. K. J., Lugaz, N., Mays, M. L., & Temmer, M. 2019, SpWea, 17, 498
Laker, R., Horbury, T. S., O'Brien, H., et al. 2024, SpWea, 22, e2023SW003628
Leitner, M., Farrugia, C. J., Möstl, C., et al. 2007, JGRA, 112, A06113
Lepping, R. P., Acũna, M. H., Burlaga, L. F., et al. 1995, SSRv, 71, 207
Lepping, R. P., Wu, C. C., & Berdichevsky, D. B. 2005, AnGeo, 23, 2687
Liu, Y. D., Hu, H., Zhao, X., Chen, C., & Wang, R. 2024, ApJL, 974, L8
Lopez, R. E. 1987, JGR, 92, 11189
Lugaz, N. 2010, SoPh, 267, 411
Lugaz, N., Farrugia, C. J., Winslow, R. M., et al. 2018, ApJL, 864, L7
Lugaz, N., Lee, C. O., Al-Haddad, N., et al. 2024b, SSRv, 220, 73
Lugaz, N., Salman, T. M., Zhuang, B., et al. 2022, ApJ, 929, 149
Lugaz, N., Zhuang, B., Scolini, C., et al. 2024a, ApJ, 962, 193
Luhmann, J. G., Gopalswamy, N., Jian, L. K., & Lugaz, N. 2020, SoPh, 295, 61
Lynch, B. J., Antiochos, S. K., Li, Y., Luhmann, J. G., & DeVore, C. R. 2009, ApJ, 697, 1918
Manchester, W., Kilpua, E. K. J., Liu, Y. D., et al. 2017, SSRv, 212, 1159
Möstl, C., Isavnin, A., Boakes, P. D., et al. 2017, SpWea, 15, 955
Neugebauer, M., & Giacalone, J. 2005, JGRA, 110, A12106
Nieves-Chinchilla, T., Vourlidas, A., Raymond, J. C., et al. 2018, SoPh, 293, 25
Odstrcil, D., & Pizzo, V. J. 1999, JGR, 104, 28225
Owens, M. J. 2020, SoPh, 295, 148
Pal, S., dos Santos, L. F. G., Weiss, A. J., et al. 2024, ApJ, 972, 94
Regnault, F., Al-Haddad, N., Lugaz, N., et al. 2023, ApJ, 957, 49
Regnault, F., Al-Haddad, N., Lugaz, N., et al. 2024, ApJ, 962, 190
Richardson, I. G., & Cane, H. V. 2004, JGRA, 109, A09104
Richardson, I. G., & Cane, H. V. 2010, SoPh, 264, 189
Rodriguez, L., Mierla, M., Zhukov, A. N., West, M., & Kilpua, E. 2011, SoPh, 270, 561
Rouillard, A. P., Lavraud, B., Sheeley, N. R., et al. 2010, ApJ, 719, 1385
Salman, T. M., Lugaz, N., Winslow, R. M., et al. 2021, ApJ, 921, 57
Scolini, C., Lugaz, N., Winslow, R. M., et al. 2024, ApJ, 961, 135
Scolini, C., Winslow, R. M., Lugaz, N., & Poedts, S. 2021, ApJL, 916, L15
Sonnerup, B. U. Ö., & Scheible, M. 1998, ISSIR, 1, 185
Szabo, A., Koval, A., Merka, J., & Narock, T. W. 2010, AGUFM, 2010, SM31A–1860
Thernisien, A., Vourlidas, A., & Howard, R. A. 2009, SoPh, 256, 111
Vourlidas, A., Lynch, B. J., Howard, R. A., & Li, Y. 2013, SoPh, 284, 179
Wang, Y., Wang, B., Shen, C., Shen, F., & Lugaz, N. 2014, JGRA, 119, 5117
Weiss, A. J., Nieves-Chinchilla, T., & Möstl, C. 2024, ApJ, 975, 169
Winslow, R. M., Lugaz, N., Philpott, L. C., et al. 2015, JGRA, 120, 6101
Winslow, R. M., Lugaz, N., Scolini, C., & Galvin, A. B. 2021, ApJ, 916, 94
Yashiro, S., Gopalswamy, N., Michalek, G., et al. 2004, JGRA, 109, A07105
Zhang, J., Temmer, M., Gopalswamy, N., et al. 2021, PEPS, 8, 56
Zhao, X. H., Feng, X. S., Feng, H. Q., & Li, Z. 2017, ApJ, 849, 79
Zhuang, B., Lugaz, N., Al-Haddad, N., et al. 2024, A&A, 682, A107
Zhuang, B., Wang, Y., Hu, Y., et al. 2019, ApJ, 876, 73
Zhuang, B., Wang, Y., Shen, C., et al. 2017, ApJ, 845, 117